3D Histological Analysis of Soft Tissues by Contrast-Enhanced X-Ray Microfocus Computed Tomography: Screening and Staining Optimization of Contrast-Enhancing Staining Agents

Delia Hoffmann, Tim Balcaen, Sarah Vangrunderbeeck, Léna Puigdevall Mata, Arne Maes, Grzegorz Pyka, Laure Dumoutier, Catherine Behets, Wim De Borggraeve, Greet Kerckhofs

TESCAN MIRA



FROM ROUTINE TO REMARKABLE

Downloaded from https://academic.oup.com/mam/article/31/2/ozaf013/8104027 by guest on 23 May 2025

Microscopy and Microanalysis, 2025, **31**, ozaf013
https://doi.org/10.1093/mam/ozaf013
Advance access publication 2 April 2025
Original Article

Microscopy AND Microanalysis

3D Histological Analysis of Soft Tissues by Contrast-Enhanced X-Ray Microfocus Computed Tomography: Screening and Staining Optimization of Contrast-Enhancing Staining Agents

Delia Hoffmann[1,2,3], Tim Balcaen[1,4,5], Sarah Vangrunderbeeck[4,5], Léna Puigdevall Mata[6], Arne Maes[1,5,7], Grzegorz Pyka[1,5], Laure Dumoutier[6], Catherine Behets[1], Wim De Borggraeve[4], and Greet Kerckhofs[1,3,5,7,*]

[1]*Pole of Morphology, Institute of Experimental and Clinical Research, UCLouvain, Avenue E. Mounier 52 - box B1.52.04, 1200 Brussels, Belgium*
[2]*Skeletal Biology and Engineering Research Center, KU Leuven, O&N I Herestraat 49 - box 813, 3000 Leuven, Belgium*
[3]*Prometheus, Division of Skeletal Tissue Engineering, KU Leuven, O&N I Herestraat 49 - box 813, 3000 Leuven, Belgium*
[4]*Department of Chemistry, Sustainable Chemistry for Metals and Molecules, KU Leuven, Celestijnenlaan 200 F - box 2404, 3001 Leuven, Belgium*
[5]*Biomechanics Lab, Institute of Mechanics, Materials and Civil Engineering, UCLouvain, Place du Levant 2 - box L5.04.01, 1348 Louvain-la-Neuve, Belgium*
[6]*Experimental Medicine Unit, de Duve Institute, UCLouvain, Avenue Hippocrate 74 - box B1.75.02, 1200 Brussels, Belgium*
[7]*Department of Materials Engineering, KU Leuven, Kasteelpark Arenberg 44 - box 2450, 3001 Leuven, Belgium*

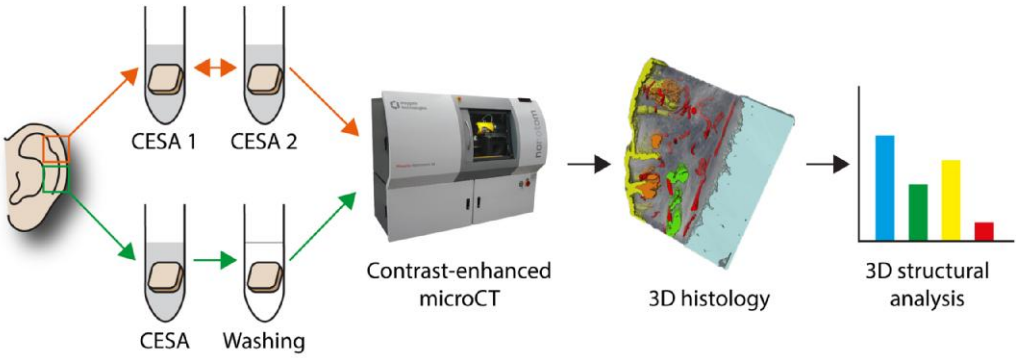
*Corresponding author: Greet Kerckhofs, E-mail: greet.kerckhofs@uclouvain.be

Abstract

The gold standard for studying biological soft tissues at the microscale (i.e., histology) is tissue sectioning with subsequent colorimetric or fluorescent staining and visual inspection under the microscope. When tissue integrity must be maintained for 3D histological assessment, contrast-enhanced microfocus X-ray computed tomography (CECT) is a promising solution, but there is still a lack of staining protocol optimization of contrast-enhancing staining agents (CESAs). Therefore, in this study, mouse auricles were incubated with Hafnium-substituted Wells–Dawson polyoxometalate, cationic iodinated contrast agent, or Lugol's iodine and were imaged with high-resolution CECT. Alignment with corresponding H&E-stained sections enabled the identification and segmentation of different tissue types. Contrast differences between tissue types were increased by washing the samples after staining or by combining CESAs. Finally, we proved that the latter could be used to quantitatively assess the 3D thickness distribution of the epidermis in the ears of a mouse model of psoriasis-like dermatitis. In conclusion, CECT and bright-field microscopy are complementary and not mutually exclusive techniques for the histological assessment of biological tissues. While bright-field microscopy gives detailed information about the cellular composition of tissues, CECT provides a better insight into the spatial interrelationship of tissues and is a powerful tool for performing 3D structural quantification.

Key words: 3D X-ray-based histology, contrast-enhanced computed tomography, contrast-enhancing staining agents, external ear

Graphical Abstract



Received: July 11, 2024. **Revised:** January 4, 2025. **Accepted:** February 26, 2025
© The Author(s) 2025. Published by Oxford University Press on behalf of the Microscopy Society of America. All rights reserved. For commercial re-use, please contact reprints@oup.com for reprints and translation rights for reprints. All other permissions can be obtained through our RightsLink service via the Permissions link on the article page on our site—for further information please contact journals.permissions@oup.com.

Downloaded from https://academic.oup.com/mam/article/31/2/ozaf013/8104027 by guest on 23 May 2025

Introduction

Studies of physiological and pathological processes often require the histological analysis of biological samples, meaning their evaluation at the microscopic level. In most clinical and preclinical laboratories, histology is conventionally studied using optical (bright-field and fluorescence) microscopy. Numerous colorimetric and fluorescent staining techniques have been developed, ranging from general stains used to assess the global cellular and extracellular matrix organization to the specific staining of a single protein. As such, hematoxylin-eosin (H&E) and Masson's Trichrome (MTC) are the most general colorimetric stains by highlighting cytoplasm, nuclei, and fibers. More specific stains include Safranin O, used to stain cartilage, or Verhoeff's stain, used to highlight elastic fibers (Titford, 2009; Musumeci, 2014). The highest specificity is conferred by antibodies, which are used to stain proteins by immunohistochemistry or immunofluorescence (Coleman, 2000; Titford, 2006). While optical microscopy provides detailed information in 2D, its ability to capture 3D microstructural information is severely restricted. Even if a sample were fully sectioned and each section stained and analyzed, which is not practical or economically feasible, the information in the third dimension would still be restricted because a classical section is 5 μm thick and the resulting voxel is not isotropic. Therefore, alternative techniques must be used when information about the 3D organization or spatial distribution of tissue structures, cells, or molecules is required.

A rapidly growing field for analyzing the spatial distribution of proteins is light-sheet microscopy, which images whole tissues stained with fluorochrome-labeled antibodies (Dyer et al., 2022). The downsides of this technique are mainly the slow diffusion of antibodies into the samples (Messal et al., 2021), the need for tissue clearing to reduce light absorption (by pigments) and scattering (by fibers, cell membrane, nucleus, organelles, and surrounding media) (Yu et al., 2021), the decalcification of mineralized samples like bone or teeth (Jing et al., 2019), and the poor visibility of the general tissue histology despite the presence of a nuclear counterstain.

X-ray microfocus computed tomography (microCT) is a structure-preserving imaging technique that circumvents some of the problems caused by fluorescence, such as light scattering or the need for decalcification, because X-rays have higher energy than visible light ("X-rays", https://www.nibib.nih.gov/science-education/science-topics/x-rays). Current *ex vivo* microCT devices can achieve voxel sizes in the range of 1 μm and have been used for several decades to study mineralized tissues, such as bone, in 3D (Waarsing et al., 2005; Deyhle et al., 2016). However, soft tissues are difficult to discriminate due to their poor and similar X-ray-attenuating properties, which emphasizes the need to stain them with contrast-enhancing staining agents (CESAs) prior to imaging, a technique referred to as contrast-enhanced microCT (CECT) (De Bournonville et al., 2019). These CESAs are compounds containing high atomic number atoms that passively diffuse into the sample to stain soft tissues (De Bournonville et al., 2019). The first application of CESAs for the examination of soft tissues dates back to the early 21st century, when osmium tetroxide was used to phenotypically and anatomically assess a mouse embryo, a porcine lung, and a honeybee brain (Johnson et al., 2006; Litzlbauer et al., 2006; Ribi et al., 2008). Due to its high toxicity, osmium tetroxide has been replaced by a variety of CESAs, which are mostly organic or inorganic molecules containing atoms with a high atomic number (e.g., iodine, tungsten, molybdenum) (Koç et al., 2019). As an alternative X-ray-based imaging technique, phase contrast imaging shows promising results (Albers et al., 2024). However, this technique is not suitable for everyday use because image acquisition is time-consuming and requires expensive synchrotron facilities or specialized microCT systems with in-line phase contrast (Kalson et al., 2012; Walsh et al., 2021).

CECT has been widely used to answer specific biomedical research questions, but to the best of our knowledge, CESAs have never been systematically compared to determine which CESA and staining protocol could be used to analyze the general histology of an organ in 3D. Therefore, we selected three previously described CESAs: Lugol's iodine (Metscher, 2009), cationic iodinated contrast agent (CA4+) (Joshi et al., 2009), and 1:2 Hafnium-substituted Wells–Dawson polyoxometalate (Hf-WD 1:2 POM) (Kerckhofs et al., 2018). The CESAs were selected for the following reasons. (i) Lugol's iodine was first used in 2009 for the anatomical study of chick embryos (Metscher, 2009). Since then, it has been applied to a wide range of organs and species, e.g., to study the human and mouse fetal anatomy (Ban et al., 2019; Dawood et al., 2020), cardiovascular structures from different species (Leyssens et al., 2021), musculoskeletal tissues (Jeffery et al., 2011), or brain and nerve anatomy (Lombardi et al., 2019; Thompson et al., 2020). (ii) CA4+ was originally developed to stain negatively charged glycosaminoglycans in cartilage (Joshi et al., 2009), but has also been shown to reveal mouse brain microstructure (Balcaen et al., 2023). (iii) Hf-WD 1:2 POM has been successfully used to study the bone marrow vasculature and adipocytes (Kerckhofs et al., 2018), mouse kidneys (de Bournonville et al., 2020), blood vessels from different species (Leyssens et al., 2023), mouse brain (Balcaen et al., 2023), human inner ear (Starovoyt et al., 2023), mouse heart, and bovine muscle (Maes et al., 2022). There are other CESAs, such as osmium tetroxide or phosphotungstic acid, but they were not included because they are often toxic or destructive (McLaughlin et al., 1946; Litzlbauer et al., 2006; Buytaert et al., 2014). In this study, these three CESAs were applied to human and mouse ears, organs selected for their histologic heterogeneity, to describe their staining patterns. Then, inspired by staining protocols for classical colorimetric stains on 2D tissue sections, the CESA staining protocols were optimized by differentiating (i.e., removing unbound or loosely bound molecules) or by combining CESAs (analogous to H&E or MTC staining) to obtain better contrast differences between tissue structures. Finally, the best protocol was used to segment the epidermis and quantify its thickness in mice suffering from psoriasis-like dermatitis.

Materials and Methods

Mouse Samples

Healthy Auricles

Mouse auricles (external ears) were used because of their histologic heterogeneity (composed of all four tissue types, i.e., epithelial, muscle, nervous, and connective tissue). Healthy auricles, used in all figures except Figure 5, were leftover tissues from Rj:NMRInu/nu mice (Janvier-Labs) that were used for other studies. The animals were housed according to the regulations of the Animalium Leuven and all procedures performed on Rj:NMRInu/nu mice were approved by

Downloaded from https://academic.oup.com/mam/article/31/2/ozaf013/8104027 by guest on 23 May 2025

the local ethics committee for Animal Research, KU Leuven (KU Leuven, project license # 160/2019).

Diseased Auricles (Imiquimod Model)

For the imiquimod model in Figure 5, IL-22RΔCter$^{wt/wt}$ and IL-22RΔCter$^{mut/mut}$ mice were generated and selected as previously described (Michiels et al., 2021). They were bred and housed under specific pathogen-free conditions at the UCLouvain animal facility. The experiment with IL-22RΔCter$^{wt/wt}$ and IL-22RΔCter$^{mut/mut}$ mice was performed in compliance with national and institutional guidelines and was approved by the local ethics committee (LA 1230653-2023/UCL/MD/031). Eight-week-old mice (five per group) were shaved behind the ears and received daily topical applications of 0.8 mg imiquimod per ear for 7 days (commercially available cream, Aldara 5%; 3 M). Ear thickness was measured daily with a caliper (Mitutoyo, Kawasaki, Japan). After 7 days, the mice were euthanized and the auricles were dissected. Per mouse, one auricle was used for CECT imaging and the other for bright-field microscopy imaging.

Human Sample

The human auricle was harvested from a deceased donor and bequeathed to the Human Anatomy Department of the UCLouvain (IRB00008535, Brussels, Belgium).

CECT Imaging

Tissue Processing

Mouse auricles were fixed in 4% formaldehyde at 4°C for 24 h and washed three times in PBS. They were cut into approximately 4 × 2 mm pieces. The human auricle was fixed in 4% formaldehyde at 4°C for 72 h, washed three times in PBS, and cut into approximately 4 × 6 mm pieces.

CESA Staining

CA4+ (5,5′-[malonylbis(azanediyl)]bis[*N*1,*N*3-bis(2-aminoethyl)-2,4,6-triiodoisophthalamide] chloride salt, $C_{27}H_{36}I_6N_{10}O_6Cl_4$) was synthesized as an HCl salt according to the previously described protocol (Stewart et al., 2017) and used at 24 mg/mL in PBS. Hf-WD 1:2 POM ($K_{16}[Hf(\alpha_2\text{-}P_2W_{17}O_{61})_2]\cdot 19H_2O$, anionic tungsten-containing contrast agent) was synthesized as previously described (Kato et al., 2006) and used at 35 mg/mL in PBS. Buffered isotonic Lugol's iodine (312 mOsm/L) was prepared as a 1:1 volume ratio of Lugol's iodine (6.474 g I_2 and 12.948 g KI per 500 mL demineralized water) and PBS. Mouse auricles were stained in 1 mL of the CESA solution (approximately 600 μL CESA per mm³ of sample). The piece of the human auricle was stained in 3.5 mL of the CESA solution (approximately 30 μL CESA per 100 mm^3 of sample). The samples were incubated with the staining solution at room temperature on a shaker plate. In Figures 1 to 3, the incubation for all CESAs took 10 days. In Figure 4, Hf-WD 1:2 POM incubation took 7 days and CA4+ incubation 8 days. In Figure 5, Hf-WD 1:2 POM incubation took 10 days and CA4+ incubation took 7 days. In case of differentiation, the samples were washed with PBS for 21 days by refreshing the PBS after 1, 4, 7, and 11 days. In case of double staining, the samples were washed with PBS for 2–11 days before the second CESA incubation.

Image Acquisition

Samples were wrapped in parafilm together with a borosilicate bead as reference material for gray value normalization, and microCT datasets were acquired by using a Phoenix NanoTom M (GE Measurement and Control Solutions) with a diamond-coated tungsten target [tungsten deposition on a chemical vapor deposition (CVD) grown diamond window/target]. Table 1 provides an overview of the acquisition parameters. A detector calibration was performed before the acquisition of the radiographs to correct for the deviation in flux within one radiograph and to ensure uniformity of the X-ray detection.

Data Processing

The datasets were reconstructed using Datos|x (GE Measurement and Control Solutions) by applying beam hardening correction of 5, an Inline Median filter (reduces noise in the volume by filtering the projections during reconstruction using a 3 × 3 median filter), an ROI-CT filter (increases the resolution of the CT dataset for a selected ROI of the object), and a Filter Volume (the volume is filtered in slices after reconstruction using the Unsharp Masking Filter). The slices were exported as 16-bit files (.tiff). The dynamic range of the gray value histogram of the reconstructed slices was optimized by using an in-house developed Matlab script and the slices were converted to 8-bit images (.jpeg) (Supplementary Fig. S1a) ("GitHub - contrast-team/greyvalue-optimization: Normalization and histogram windowing", https://github.com/contrast-team/greyvalue-optimization). When quantifying and comparing the gray values of tissue structures of different datasets, the gray value histograms of these datasets were normalized with an in-house developed Matlab script by using the borosilicate bead and parafilm as reference materials (Supplementary Fig. S1b) ("GitHub - contrast-team/greyvalue-optimization: Normalization and histogram windowing", https://github.com/contrast-team/greyvalue-optimization).

Data Visualization

DataViewer (Bruker MicroCT, Kontich, Belgium) was used to visualize and illustrate the cross-sections. Avizo (Thermo Fischer Scientific, USA) was used for 3D rendering, segmentation, and video generation.

Gray Value Measurements

The gray values were measured using DataViewer (Bruker MicroCT). In each dataset, four slices were selected for quantification. Each slice had to contain each tissue structure of interest (epidermis, dermis, muscle, adipose tissue, and cartilage), and the slices were spaced 50 slices apart. On each slice, each tissue structure was quantified twice by drawing two lines of a maximum of 100 voxels. Each line resulted in a histogram with one gray value per voxel (Supplementary Fig. S2a). The mean gray value per line was calculated, and then, the mean of the eight lines per tissue structure per dataset was calculated. This strategy worked well for the epidermis, dermis, and muscle due to their homogeneous staining. However, in cartilage and adipose tissue, the individual voxel values were spread over a wide range of gray values because of the inhomogeneous staining of these structures. Specifically, in cartilage, lacunae and matrix had different gray values, whereas in adipose tissue, adipocytes and extracellular matrix were differently stained (Supplementary Fig. S2a). Therefore, only a fraction of the histogram was selected to calculate the mean

Downloaded from https://academic.oup.com/mam/article/31/2/ozaf013/8104027 by guest on 23 May 2025

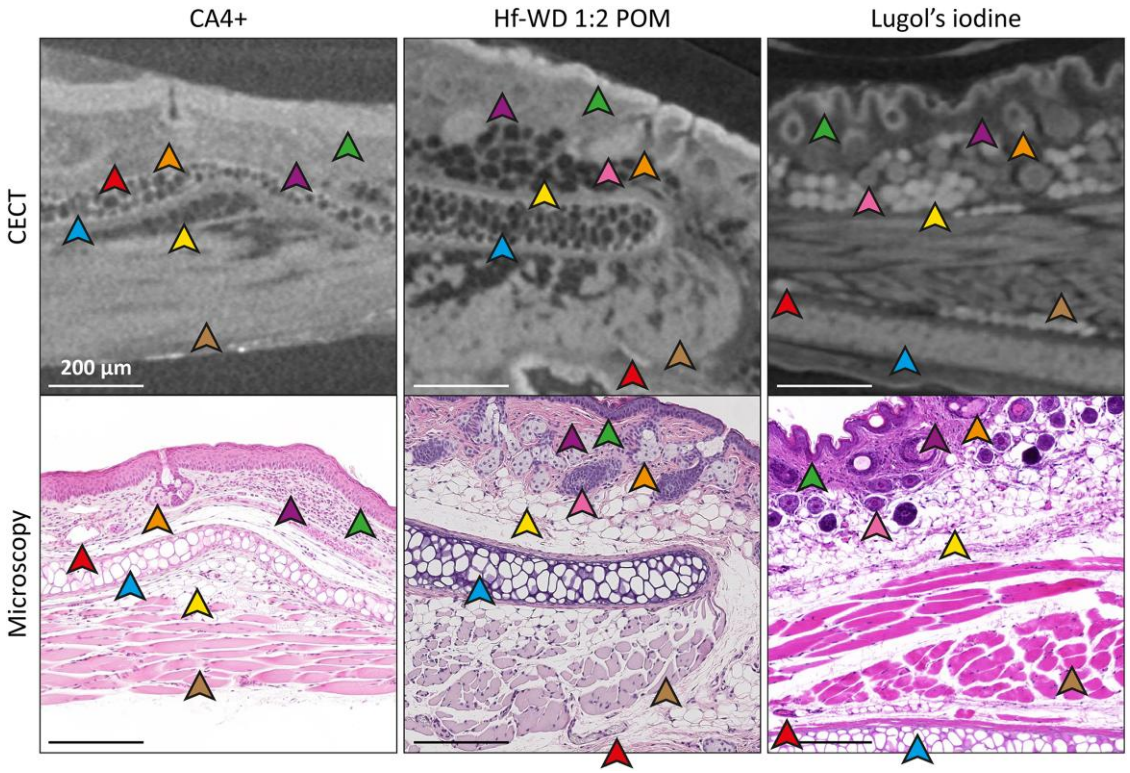


Fig. 1. Identification of tissue types and cells in CECT datasets of mouse auricles. Fixed mouse auricles were stained with CA4+, Hf-WD 1:2 POM, or Lugol's iodine, imaged with microCT, embedded in paraffin, sectioned, stained with H&E, and scanned with a slide scanner. The gray values of the CECT datasets were individually optimized. CECT and microscope images were manually aligned. Green = epidermis, purple = dermis, orange = sebaceous glands, pink = hair follicles, red = blood vessels, yellow = adipose tissue, brown = skeletal muscle, blue = elastic cartilage.

gray value (Supplementary Fig. S2b). For example, Hf-WD 1:2 POM and CA4+ were excluded from adipocytes but stained the extracellular matrix. To quantify the gray values of the adipocytes, only the bottom 30% of the gray value histogram was selected. The opposite was done for Lugol's iodine-stained adipose tissue. The top 30% of the gray value histogram was selected because the adipocytes stained more intensely than the surrounding connective tissue. For cartilage, the top 30% of the gray value histograms was selected for all three CESAs, i.e., extracellular matrix for Hf-WD 1:2 POM and CA4+ and lacunae for Lugol's iodine.

Quantification of Epidermal Thickness

First, the epidermis was segmented using Avizo 2022.1 (Thermo Fischer Scientific, USA). Segmentation began by filtering the datasets with Unsharp Masking (Edge Size 20 px, Edge Contrast 1, Brightness Threshold 0) and Non-Local Means (Spatial Standard Deviation 3, Intensity Standard Deviation 0.3, Search Window 10 px, Local Neighborhood 3). The epidermis was then segmented in five steps. (i) The epidermis was roughly selected by manually surrounding it on 1 out of 10 slices in imiquimod-treated mice or on 1 out of 3 slices in control mice. More slices were needed for control mice because the control epidermis was much thinner than the imiquimod-treated epidermis. Otherwise, the interpolation performed in the next step would fail. (ii) These manually drawn regions of interest (ROIs) were interpolated to the other slices and manually corrected. Thanks to this interpolation, the entire epidermis was selected, regardless of whether the manual surrounding in step (i) was performed on 1 out of 3 or 10 slices. (iii) The more accurate segmentation of the epidermis was done by region growing based on gray values (*magic wand* tool). (iv) Speckles were eliminated and other imprecisions were manually removed from the segmentation. (v) The segmented epidermis was saved as a new dataset (.bmp). This segmentation was done on a volume of interest (VOI) of 800–1000 slices for imiquimod-treated mice and on a VOI of 300 slices for control mice. The VOI for control mice was smaller because the manual drawing in the first step had to be done on three times more slices. Second, the software CT Analyser (Bruker MicroCT, Belgium) was used to perform a structure thickness distribution analysis. Third, Avizo was used for 3D rendering and illustration of the thickness distribution in 3D.

Bright-field Microscopy

Tissue Processing, Sectioning, and Staining

Samples were embedded in paraffin by using a Vacuum Infiltration Tissue Processor (Tissue-Tek VIP). Five-micrometer thick sections were cut on a microtome, deparaffinized, and progressively rehydrated. For H&E staining, the sections were stained with hematoxylin (10 min), washed in running tap water (10 min), rinsed in demineralized water, dehydrated in 50 and 70% ethanol (1 min each), stained with alcoholic eosin Y (2 min), and rinsed in 70 and 100% ethanol. For MTC staining, the sections were stained with hematoxylin (10 min), washed in running tap water (10 min), rinsed in demineralized water, stained with 0.1% Fuchsin Ponceau (3 min), rinsed in demineralized water, differentiated with 1% phosphomolybdic acid (5 min), rinsed in demineralized water, stained with 1%

Downloaded from https://academic.oup.com/mam/article/31/2/ozaf013/8104027 by guest on 23 May 2025

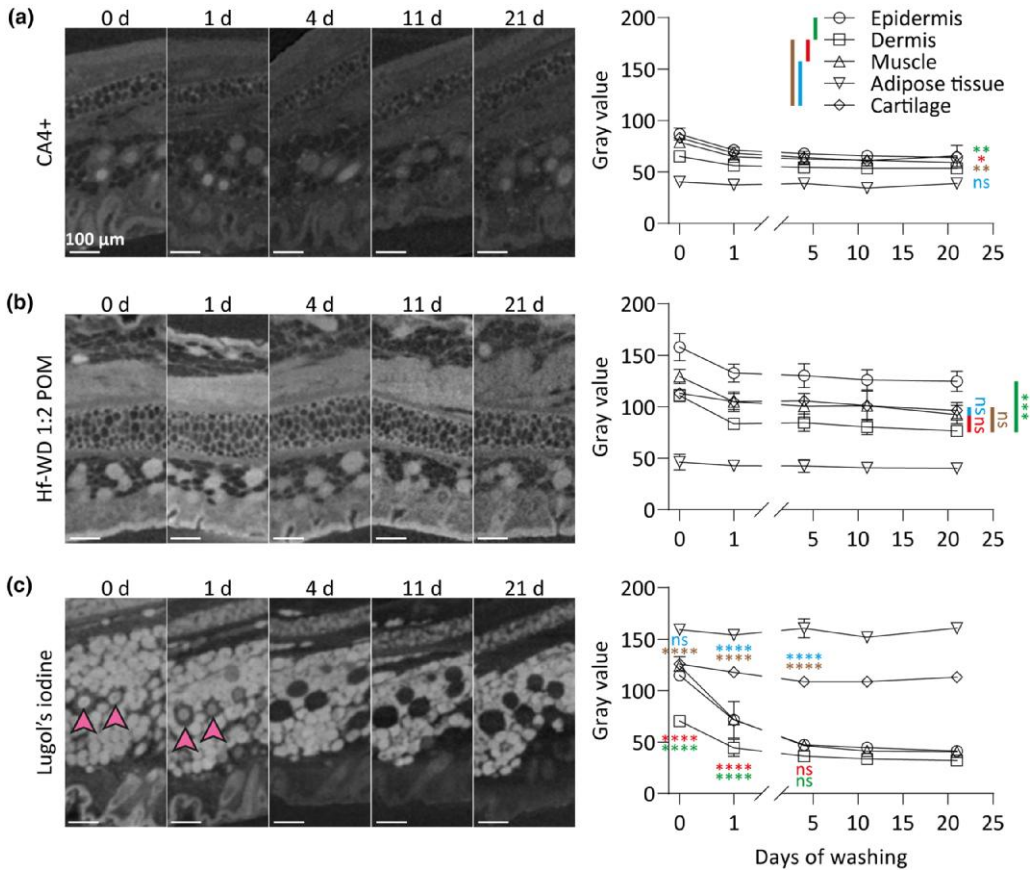


Fig. 2. Impact of washing on contrast differences between the tissues. Fixed mouse auricles were stained with CA4+ (**a**), Hf-WD 1:2 POM (**b**), or Lugol's iodine (**c**) and imaged with microCT before (=0 days) and after washing ($n = 2$–3 from one to two independent experiments). The gray values of the CA4+ and Hf-WD 1:2 POM datasets were normalized to Hf-WD 1:2 POM at day 0 thanks to two reference materials (a borosilicate bead and parafilm). The gray values of the Lugol's iodine datasets were normalized to Lugol's iodine at day 0 thanks to two reference materials (a borosilicate bead and parafilm). CECT datasets were manually aligned and gray values of epidermis, dermis, muscle, adipose tissue, and cartilage were measured. For statistical analysis, a mixed-effects analysis was applied followed by Tukey's multiple comparison test. Green = epidermis versus dermis, red = muscle versus dermis, blue = cartilage versus muscle, brown = cartilage versus dermis, pink arrowheads = hair follicles.

aniline blue (3 min), rinsed twice in demineralized water, differentiated with 1% phosphomolybdic acid (5 min), and rinsed twice in demineralized water. The sections were dehydrated, the coverslips were mounted with the Entellan new mounting medium, and the sections were digitized using the Pannoramic SCAN II slide scanner (3DHISTECH).

Quantification of Epidermal Thickness

Using CaseViewer (3DHISTECH), the epidermal thickness was manually measured at 50–100 locations on one H&E-stained tissue section per sample as previously described (Michiels et al., 2021).

Statistical Analysis

Statistical analyses were performed using GraphPad Prism 9 (GraphPad Software, USA). When more than two repeated measures of at least two groups were compared, a mixed-effects analysis followed by Tukey's multiple comparison test ($\alpha = 0.05$) was used. When comparing two groups with unpaired data, a Mann–Whitney test ($\alpha = 0.05$) was used. When comparing two groups with paired data, a Wilcoxon matched-pairs signed rank test was used (ns = not significant, $^{*}p < 0.05$, $^{**}p < 0.01$, $^{***}p < 0.001$, $^{****}p < 0.0001$). Bar and line graphs show the mean ± standard deviation (SD).

Results

CECT Enables Histological Analysis of the Different Tissue Types in Mouse Auricles

The CESAs (Lugol's iodine, CA4+, and Hf-WD 1:2 POM) were tested for their ability to reveal the histology of mouse auricles (external ears) in full 3D using CECT imaging. The mouse auricle was selected as a working model because it is a heterogeneous organ composed of all four tissue types, i.e., epithelial, muscle, nervous, and connective tissue, and would therefore provide a maximum of information in a single sample. The samples were stained with either CESA, imaged by CECT, and subsequently processed for bright-field microscopy (Fig. 1). By aligning CECT slices and microscope images, several tissue structures could be identified with all three CESAs, such as the epidermis (green arrows), dermis (purple arrows), sebaceous glands (orange arrows), hair follicles (pink arrows), adipose tissue (yellow arrows), cartilage (blue arrows), and blood vessels (red arrows). Hence, CECT and bright-field microscopy (H&E staining) provided similar information regarding tissue types and structures. Once the structures were identified through the alignment with microscope images, the structures could be identified in other datasets without the help of microscopy.

Although in CECT, no individual cells could be identified except for adipocytes and elastic cartilage lacunae (Fig. 1), it

Downloaded from https://academic.oup.com/mam/article/31/2/ozaf013/8104027 by guest on 23 May 2025

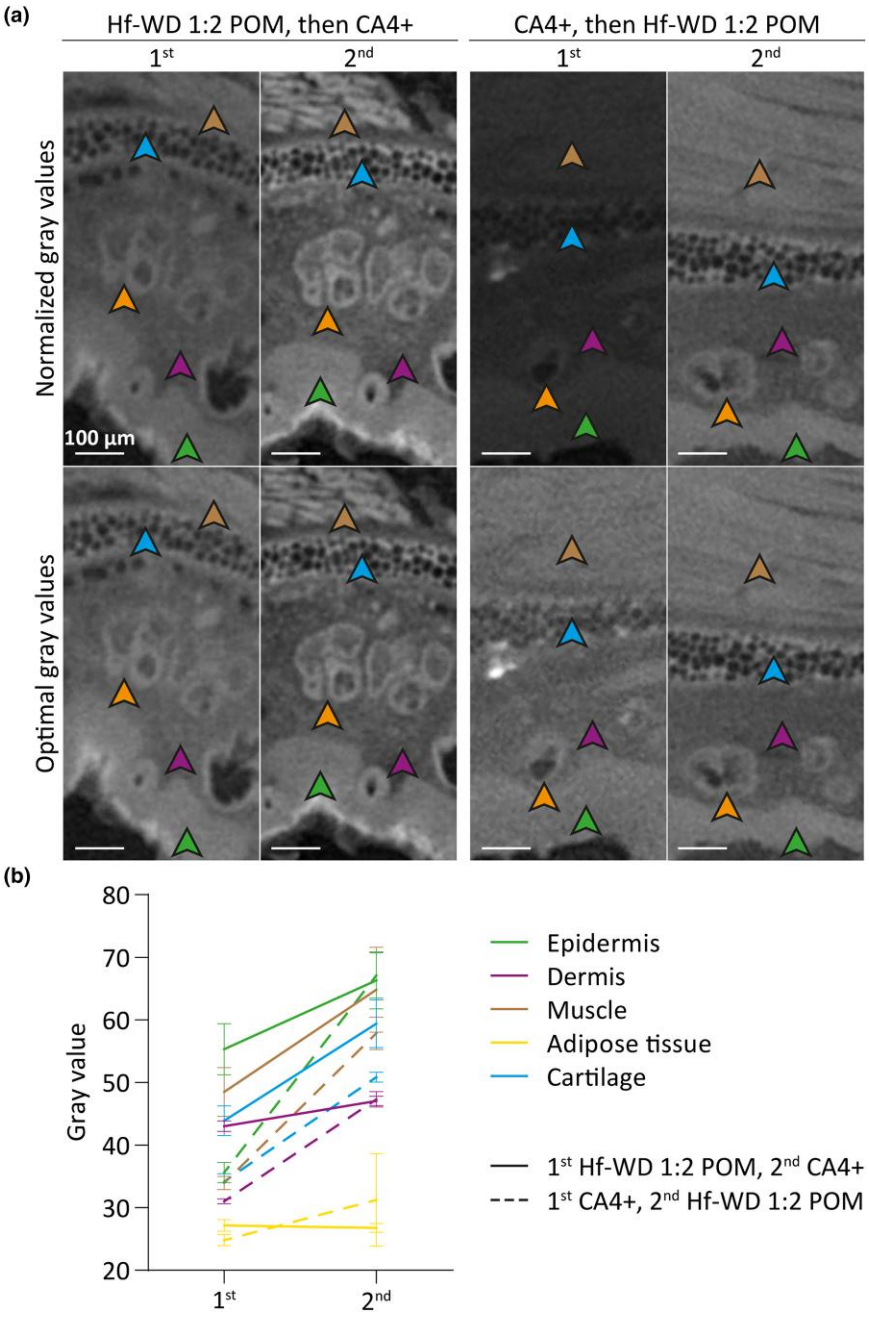


Fig. 3. Impact of double staining on contrasts. Fixed mouse auricles were stained with a first CESA, either Hf-WD 1:2 POM or CA4+, and imaged with microCT. The samples were then washed with PBS and stained with a second CESA, CA4+, or Hf-WD 1:2 POM, respectively, and imaged a second time. The gray values were normalized (reference = second dataset of CA4+ after Hf-WD 1:2 POM) or individually optimized. (**a**) CECT datasets were manually aligned. Green = epidermis, purple = dermis, orange = sebaceous glands, brown = skeletal muscle, blue = elastic cartilage. (**b**) Gray values of epidermis, dermis, muscle, adipose tissue, and cartilage ($n = 3$ from two independent experiments) were measured on the normalized datasets. For statistical analysis, each tissue type was individually analyzed. A Mann–Whitney test was applied to compare both combinations after the second staining. The results were not statistically significant.

had the advantage over H&E staining in that it was less labor-intensive, tissue-preserving, and the sample could be viewed in any direction.

While all CESAs revealed the ear microstructure, they displayed some major differences. First, the staining patterns were not the same. The most important difference was in adipocytes and cartilage lacunae. While CA4+ and Hf-WD 1:2 POM were excluded from these two structures, they were stained with Lugol's iodine (Fig. 1). Second, the CESAs produced different staining intensities (Supplementary Fig. S3). In Figure 1, the gray values were optimized individually for each CECT dataset, but when normalized by means of two reference materials, it became obvious that the Lugol's iodine staining was much more intense than Hf-WD 1:2 POM and CA4+ (Supplementary Fig. S3). However, the comparison of their gray values should be handled with caution because the acquisition parameters were not exactly the same for the three CESAs.

Downloaded from https://academic.oup.com/mam/article/31/2/ozaf013/8104027 by guest on 23 May 2025

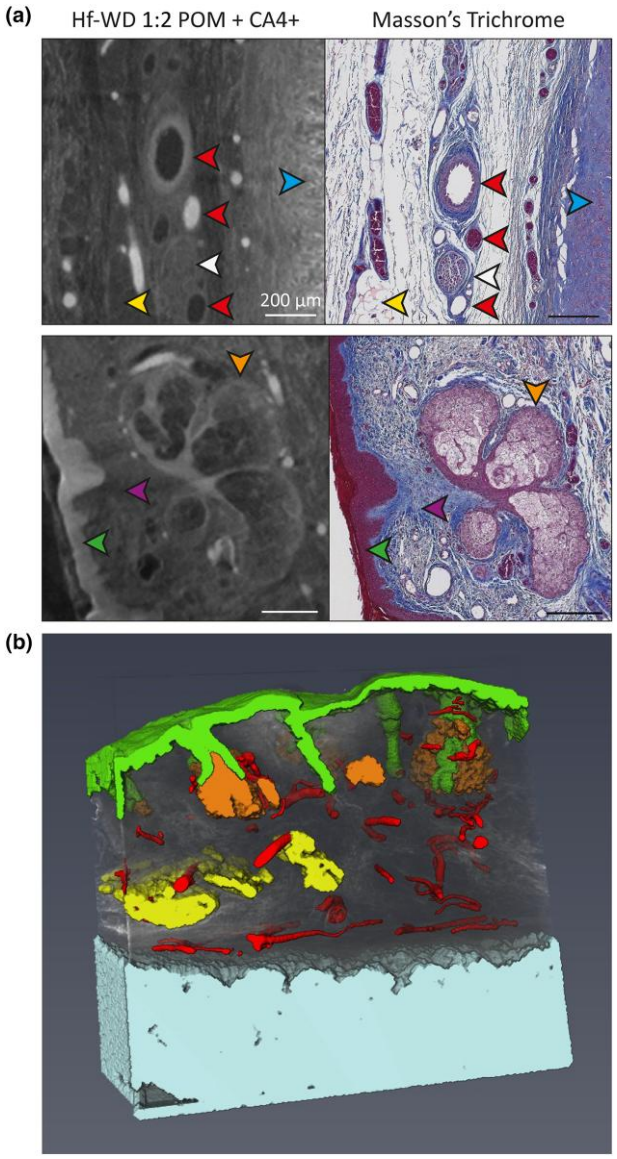


Fig. 4. 3D visualization of tissue types of the human ear. A fixed human auricle was double-stained with Hf-WD 1:2 POM followed by CA4+, imaged with microCT, embedded in paraffin, sectioned, stained with Masson's Trichrome, and scanned with a slide scanner. (**a**) CECT and microscope images were manually aligned. (**b**) The epidermis, sebaceous glands, adipose tissue, veins filled with blood cells, and cartilage were segmented and 3D rendered (corresponding video in Video 1). Green = epidermis, purple = dermis, orange = sebaceous glands, red = vessels (top arrow = empty artery, middle arrow = vessel filled with blood cells, bottom arrow = empty vein), yellow = adipose tissue, blue = elastic cartilage, white = nerve.

Differentiation After CESA Staining Improves Contrast Differences Between Tissue Structures

The images in Figure 1 were obtained by simply incubating the organ in the CESA solution. In comparison, staining protocols of classical colorimetric stains for tissue sections often include washing steps. The samples are first overstained and then the unbound or loosely bound molecules are removed to increase the contrast difference between tissue structures, a principle called differentiation. To determine if CESA-stained auricles could benefit from differentiation, the auricles were washed with PBS, the CESA's solvent, after staining. The final image quality of Hf-WD 1:2 POM- and CA4+-stained samples was little affected by washing because, after 21 days of washing, all the tissue structures could still be identified (Figs. 2a, 2b). This observation was confirmed by quantifying the gray values of different tissue types before and after differentiation. The staining intensities of both CESAs decreased slightly and similarly for all tissue types during the first day of washing but quickly stabilized thereafter (Figs. 2a, 2b). CA4+ staining decreased most in the epidermis (26%) and Hf-WD 1:2 POM in the dermis (31%) (Supplementary Table S1). Lugol's iodine behaved differently depending on the tissue type. While adipocytes and cartilage were unaffected, up to 70% of the stain was removed from the epidermis, hair follicles, dermis, and muscle (Fig. 2c, Supplementary Table S1). Therefore, differentiation with PBS proved to be useful to discriminate cartilage from surrounding tissues or to identify adipocytes with Lugol's iodine, which could be mistaken with hair follicles prior to washing due to similar shapes and staining intensities (Fig. 2c, pink arrows).

Double Staining Improves Contrast Differences Between Tissue Types

Another technique used to improve contrast differences between tissues in classical colorimetric staining protocols for tissue sections is the combination of stains, such as the combination of Mayer's hematoxylin (nuclei) and eosin (cytoplasm) for H&E staining. We evaluated the added value of combining CA4+ and Hf-WD 1:2 POM. Mouse auricles were subsequently stained with CA4+ and Hf-WD 1:2 POM, or vice versa. Visual inspection of the images showed that the combination of CESAs improved the contrast difference between tissue types, especially between the epidermis or muscle and the surrounding connective tissue proper (Fig. 3a). Quantification of the gray values confirmed a general increase after the second staining for all tissue types, except for adipocytes (Fig. 3b, Supplementary Table S2). This increase was less pronounced in the dermis (Supplementary Table S2). More precisely, when Hf-WD 1:2 POM was followed by CA4+ (first combination), the dermis increased by 9% whereas the epidermis and muscle increased by 20 and 33%, respectively. When CA4+ was followed by Hf-WD 1:2 POM (second combination), the dermis increased by 53% whereas the epidermis and muscle increased respectively by 88 and 71% (Supplementary Table S2). This may explain why the borders between the dermis and other tissue types such as epidermis, muscle, or glands were better defined when combining CESAs (Fig. 3a). Based on the increase in gray value intensity of most tissue types, it may seem that the second combination (CA4+ followed by Hf-WD 1:2 POM, e.g., 88% in the epidermis) was better than the first combination (Hf-WD 1:2 POM followed by CA4+, e.g., 20% in the epidermis), but it must be kept in mind that the absolute values, in the end, were the same for epidermis and dermis (Fig. 3b, Supplementary Table S3). The gray values of muscle and cartilage were even higher for the first combination (Hf-WD 1:2 POM followed by CA4+), although the results were not statistically significant (Fig. 3b, Supplementary Table S3). Altogether, the first combination (Hf-WD 1:2 POM followed by CA4+) seemed to be better because visually, the differences between the tissue types were better defined, and quantitatively, muscle and cartilage had higher gray values compared with the second combination.

Downloaded from https://academic.oup.com/mam/article/31/2/ozaf013/8104027 by guest on 23 May 2025

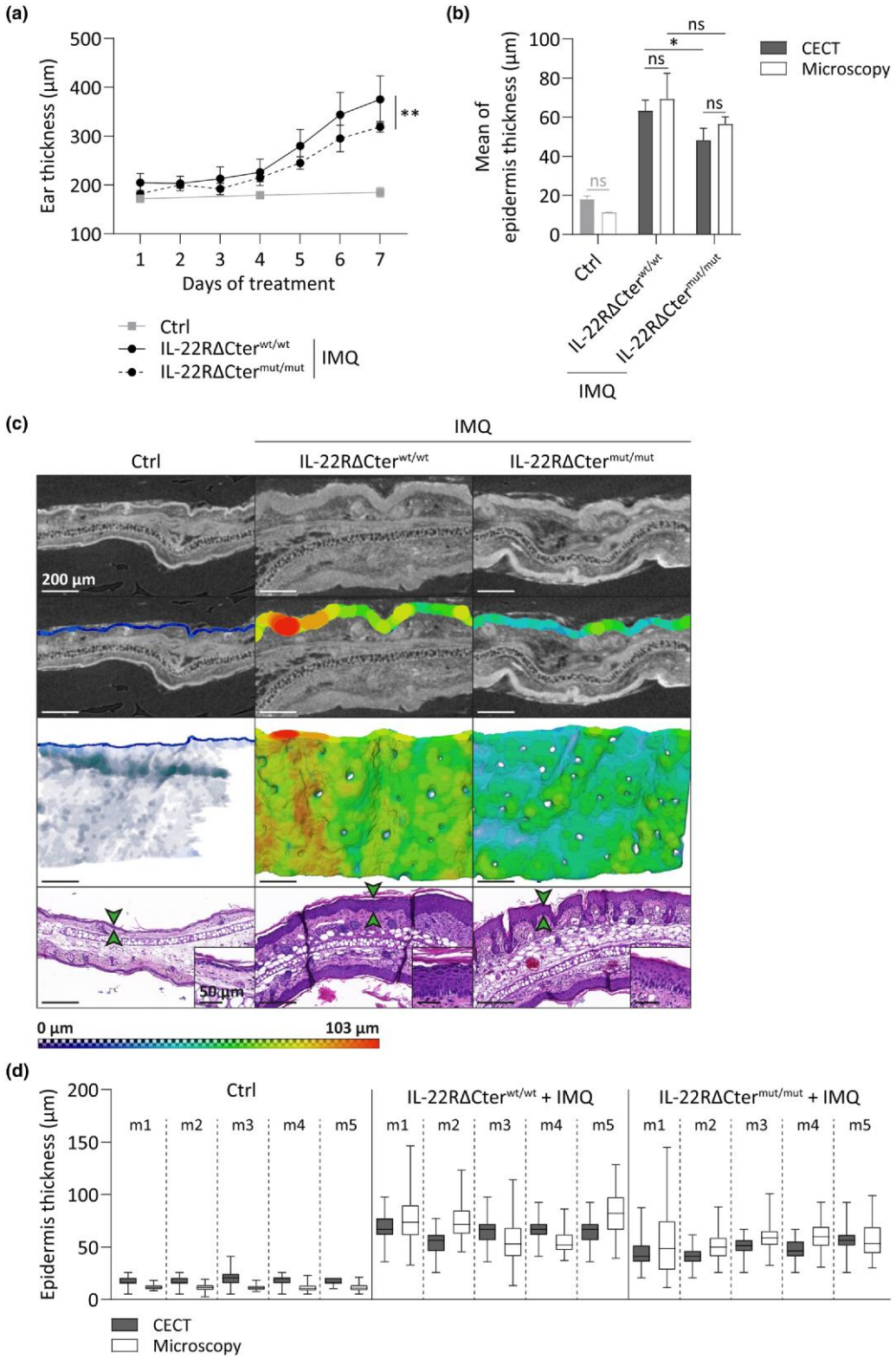


Fig. 5. Measurement of epidermal thickness by CECT and microscopy. (**a**) Ear thickness of imiquimod-treated or untreated mice ($n = 5$ per group). IL-22RΔCter$^{wt/wt}$ and IL-22RΔCter$^{mut/mut}$ mice were compared with a mixed-effects analysis. (**b**) Epidermal thickness of imiquimod-treated or untreated mice ($n = 5$ per group). From each mouse, both auricles were harvested, fixed, and analyzed. The first auricle was imaged by CECT with Hf-WD 1:2 POM followed by CA4+ and the epidermal thickness was quantified. The second auricle was processed for H&E staining and epidermal thickness analysis. For statistical analysis, the groups were compared in pairs. For comparisons between techniques (paired data), a Wilcoxon matched-pairs signed rank test was applied. For comparisons between treatments (unpaired data), a Mann–Whitney test was applied. (**c**) Representative images were selected for transverse sections of the CECT datasets (first line), the same images with the segmented epidermis (second line), and the surface view of the segmented epidermis in 3D (third line). The segmented epidermis was color-coded, with blue representing the thinnest regions and red the thickest regions. Representative images of the HE-stained epidermis were selected (fourth line). The epidermis is located between two green arrows. (**d**) Box plot representation of the epidermal thickness measurements per mouse (m).

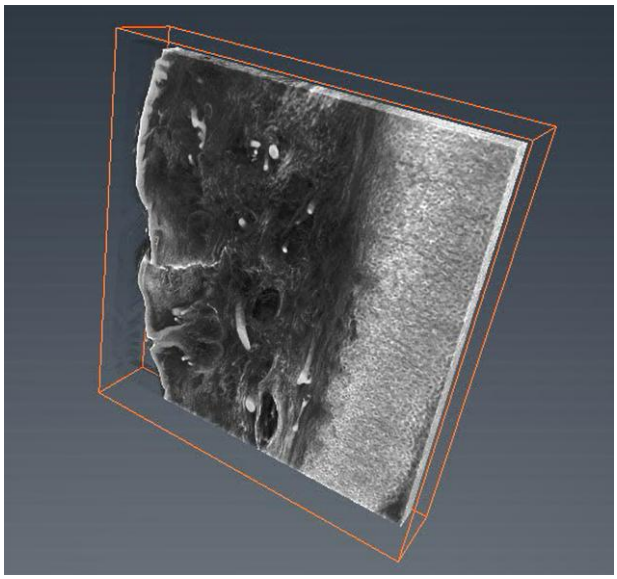
Downloaded from https://academic.oup.com/mam/article/31/2/ozaf013/8104027 by guest on 23 May 2025

Table 1. MicroCT Acquisition Parameters.

Figure	Figures 1 to 3: Hf-WD 1:2 POM and CA4+	Figure 1: Lugol's iodine	Figure 2: Lugol's iodine	Figure 4	Figure 5
Voxel size (μm)	2.57	2.80	2.57	3.00	2.57
Source voltage (kV)	60	60	75	70	60
Tube current (μA)	181	197	144	180	181
Focal spot size (μm)	2.57	2.8	2.56	2.98	2.57
0.1 mm Al filter	Yes	Yes	Yes	Yes	Yes
Exposure time (ms)	500	500	500	500	500
# Projections	2,400	2,400	2,400	1,600	2,400
Detector size (pixels)	3,072 × 2,400	3,072 × 2,400	3,072 × 2,400	3,072 × 2,400	3,072 × 2,400
Average	3	3	3	2	1
Skip	1	1	1	1	0
Total acquisition time	1 h 26 m	1 h 26 m	1 h 26 m	40 m	20 m

CECT Enables the Simultaneous 3D Rendering of Multiple Tissue Structures

3D histological analysis requires not only a good staining and acquisition protocol but also the subsequent segmentation of the structure of interest. For this purpose, the contrast differences between the tissues should be as high as possible. As a proof of concept, a human auricle was co-stained with Hf-WD 1:2 POM followed by CA4+ because this combination allowed the best discrimination between dermis and epidermis or glands (Fig. 3a). First, the structures of interest were identified by aligning the CECT dataset with a corresponding MTC-stained section (Fig. 4a). In addition to epidermis, dermis, sebaceous glands, cartilage, and adipose tissue, which had already been detected in mouse auricles (Fig. 1), additional structures such as nerves and different types of vessels (empty arteries and veins or veins filled with blood cells) could be identified (Fig. 4a). Thanks to the good contrast differences between the tissue types, epidermis (green), sebaceous glands (orange), adipose tissue (yellow), veins filled with blood cells (red), and cartilage (blue) could then be segmented, visualized in 3D and digitally assessed (Fig. 4b, Video 1). Technically challenging in bright-field microscopy, segmentation and 3D visualization of tissue types are an important added value of CECT imaging.



Video 1. 3D visualization of tissue types of the human ear. Video of the spatial distribution of epidermis (green), sebaceous glands (orange), adipose tissue (yellow), veins filled with blood cells (red), and cartilage (blue) in a human auricle double-stained with Hf-WD 1:2 POM followed by CA4+ (segmentation and 3D rendering done in Fig. 4b).

CECT Enables a Full 3D Structural Analysis of Tissues

To demonstrate the added value of 3D X-ray-based histology compared with optical microscopy, the staining protocol with the best contrast differences between tissue types, Hf-WD 1:2 POM followed by CA4+, was applied to a mouse model of imiquimod-induced psoriasis-like dermatitis. Imiquimod treatment causes epidermal thickening, which has been measured and quantified so far by paraffin embedding, tissue sectioning, and manual measurement of epidermal thickness or counting of the cell layers at different locations on the sections (Van Belle et al., 2012; Cochez et al., 2017). Here, we used mice with a truncated IL-22 receptor (IL-22RΔCter$^{mut/mut}$), which are known to be less sensitive to imiquimod-induced epidermal thickening than WT mice (IL-22RΔCter$^{wt/wt}$) (Michiels et al., 2021). First, the measurement of the ear thickness throughout the imiquimod treatment showed that IL-22RΔCter$^{mut/mut}$ ears were slightly thinner than IL-22RΔCter$^{wt/wt}$ ears (Fig. 5a), confirming that IL-22RΔCter$^{mut/mut}$ mice were less sensitive to imiquimod-induced dermatitis (Michiels et al., 2021). Second, CECT and microscope images and their structural quantifications confirmed the tendency of imiquimod-induced epidermal thickening (Figs. 5b, 5c). However, only CECT provided statistically significant results between IL-22RΔCter$^{wt/wt}$ and IL-22RΔCter$^{mut/mut}$ mice because of smaller standard deviations on the average thickness for the same number of samples (Fig. 5b). Third, we observed that the standard deviation of the individual thickness measurements within a sample was smaller for the CECT distribution analysis than for the microscopy measurements (Fig. 5d), meaning that CECT provided more accurate results. Altogether, the data showed that both techniques could be used to quantify tissue structures, although only the 3D quantification provided statistically significant results. In addition, only CECT imaging provided a 3D rendering and representation of the thickness distribution of the epidermis, which allowed a better understanding of local differences and heterogeneity in the treatment (third line in Fig. 5c).

Discussion

CECT imaging with CESAs has been extensively used to study biomedical research questions from an anatomical point of

Downloaded from https://academic.oup.com/mam/article/31/2/ozaf013/8104027 by guest on 23 May 2025

view (Ban et al., 2019; Lombardi et al., 2019; Dawood et al., 2020). However, histological analyses have been performed to a lesser extent (Busse et al., 2018; Kerckhofs et al., 2018; De Clercq et al., 2019; Maes et al., 2022), and little is known about the ability of CESAs to reveal the general histology of a complex organ composed of multiple tissue types, as conventionally done by optical microscopy on tissue sections stained, for example, with H&E.

We showed that Hf-WD 1:2 POM, CA4+, and Lugol's iodine can be used to study 3D X-ray-based histology of the external ear, selected for its histological heterogeneity. These CESAs enabled the detection and identification of all major tissue types. However, certain small structures, e.g., nerves in mouse auricles, or the different layers of tissue types, e.g., the stratum corneum, stratum lucideum, stratum granulosum, stratum spinosum, and stratum basale in the epidermis of the human ear, remained invisible (Figs. 1 and 4). Small vessels were impossible to detect without alignment with the microscope image, probably because of insufficient contrast resolution, which is the ability to distinguish two adjacent voxels based on differences in their gray values. Individual cells were also indistinguishable, except for adipocytes and elastic cartilage lacunae thanks to their large size and sufficient contrast resolution with the surrounding tissue (Figs. 1 and 4). The spatial resolution used in these experiments may not be sufficient to detect individual cells (Yamazaki et al., 2018). In addition, the contrast differences with the surrounding tissues or neighboring cells provided by the CESAs may not be sufficient to distinguish individual cells or small structures. In 2D bright-field or fluorescence microscopy, this contrast difference is provided by a counterstain (usually nuclear).

Under healthy conditions, the epidermis of the mouse ear is composed of approximately three cell layers (Van Belle et al., 2012). However, we observed important differences in the epidermal thickness between the CESAs (Fig. 1), most likely because the CECT images and tissue sections were not perpendicular to the epidermis. Alternatively, CESAs are known to induce structural modifications. As such, Lugol's iodine and CA4+ can cause tissue shrinkage, whereas Hf-WD 1:2 POM can cause a slight tissue swelling or be inert with respect to volume changes, depending on the organ (Vickerton et al., 2013; Buytaert et al., 2014; Maes et al., 2022; Balcaen et al., 2023; Leyssens et al., 2023). Unfortunately, evaluating CESA-caused volume changes on tissue structures is technically complicated because the reference values cannot be determined in an unstained sample. Alternatively, CECT data could be compared with the gold standard, which is bright-field microscopy, but it is important to note that paraffin embedding causes tissue shrinkage (Maes et al., 2022; Leyssens et al., 2023).

In addition to volume changes, CESAs can cause chemical changes in biological tissues, such as iodination of amino acids by Lugo's iodine (Early et al., 2020). However, this issue is not a limiting factor for our experiments as the samples are not used for further biochemical analysis such as PCR or western blot.

However, the above-mentioned limitations (missing contrasts, resolution, and structural modifications caused by CESAs) are compensated by the numerous advantages of CECT. Compared with bright-field microscopy, this technique is structure-preserving, less labor-intensive, and provides a 3D image of the sample, allowing it to be viewed from all directions in a single microCT dataset.

To improve the contrast differences between tissue structures in this study, the samples were differentiated after CESA staining (Fig. 2). The contrast differences between tissue types for Hf-WD 1:2 POM- and CA4+-stained samples were only mildly affected by washing with PBS, possibly because (i) the nature and concentration of the salts in the solution only slightly impacted the interaction of the CESA with the tissues (Kang et al., 2020) or (ii) the CESAs were strongly bound in the tissue and were physically less able to freely dissolve in and out after they entered the tissue (Hanly et al., 2023). In contrast to Hf-WD 1:2 POM and CA4+, Lugol's iodine was removed to up to 70% from most tissue types by differentiation, except for adipocytes and cartilage lacunae (Fig. 2, Supplementary Table S1), which could be explained by two different hypotheses. First, adipocytes, ageing lacunae, and chondrocytes are filled with lipids (Stockwell, 1965; Sanzone & Reith, 1976). Iodine is poorly soluble in PBS (or aqueous solutions) and therefore, redistribution from the hydrophobic to the aqueous phase would be very small. Also, iodine forms to a certain extent covalent bonds with unsaturated double bonds in fatty acids, which would not readily be cleaved in the absence of water or other nucleophilic species (Bock et al., 2021). Our second hypothesis is that chondrocytes are filled with glycogen (Sanzone & Reith, 1976). If the local concentrations of iodine species (especially iodine and triiodide) are high, polyiodides could be formed that interact with long sugars such as glycogen (Thoma & French, 1960; Cesàro et al., 1992; Brust et al., 2020).

We showed that tissue structures such as epidermis, glands, and muscle could be more easily identified when Hf-WD 1:2 POM and CA4+ were combined because the contrast difference with the surrounding connective tissue proper was increased (Fig. 3). The images also indicated that the staining order was important for muscle and cartilage. Their gray values were higher and their identification was easier when CA4+ followed Hf-WD 1:2 POM (Fig. 3). This was just a tendency, but it could become statistically significant with a bigger number of samples. The reason for this improved contrast difference remains, however, unknown. More elaborate analyses will be needed to find out if Hf-WD 1:2 POM and CA4+ bind to the tissue independently or if they interact. The latter may explain why the order of staining is important. Since CA4+ contains iodine and Hf-WD 1:2 POM contains tungsten and phosphorus, they could be distinguished by spectral imaging, and we could verify which tissues would be more stained by CA4+ and which one by Hf-WD 1:2 POM. Combining CESAs could become important in the future when structures such as the epidermis or muscle with low contrast differences compared with their surrounding tissues need to be segmented, rendered, and structurally quantified.

The importance of CECT becomes, among other reasons, apparent when the volume or the 3D spatial distribution of tissue structures needs to be quantified. While most researchers rely on 2D quantification on a limited number of tissue sections, the results can be biased by, for example, the section plane, missing information from the unanalyzed sections, and tissue shrinkage caused by paraffin embedding. To demonstrate that CECT can be used to quantify tissue structures, we applied the Hf-WD 1:2 POM and CA4+ double staining to a mouse model of psoriasis-like dermatitis in which epidermal thickening had been beforehand validated by manual measurements on bright-field microscopic images (Michiels et al., 2021). We confirmed that the difference in epidermal thickness between IL-22RΔCter$^{wt/wt}$ and IL-22RΔCter$^{mut/mut}$ could be measured by CECT. However, the manual

Downloaded from https://academic.oup.com/mam/article/31/2/ozaf013/8104027 by guest on 23 May 2025

measurement on microscope images did not give statistically significant results in our hands (Fig. 5b). As we used five mice per group instead of eight (Michiels et al., 2021), we hypothesize that CECT provides statistically significant results with smaller sample sizes compared with microscopy imaging. Interestingly, we also observed that the standard deviation of the individual thickness measurements was smaller in the CECT distribution analysis compared with the microscopy measurements (Fig. 5d), probably because more data points were analyzed and because the CECT analysis was not influenced by selection and orientation bias of the tissue sections. In addition, CECT imaging allowed the full 3D thickness visualization of the samples, revealing inhomogeneous effects that were not visible on 2D sections (Fig. 5c).

Conclusion

In conclusion, we have improved staining protocols for CECT by washing and combining different CESAs. These improvements are important when structures with low contrast differences compared with their surrounding tissues need to be segmented, rendered, and structurally quantified. We have also shown that CECT and bright-field microscopy are complementary and not mutually exclusive techniques for the histological assessment of biological tissues. While bright-field microscopy gives detailed information about the cellular composition of the tissue, CECT provides a better insight into the spatial interrelationship of tissues and is a powerful and structure-preserving tool to perform structural quantifications.

Availability of Data and Materials

The datasets generated and/or analyzed in the current study are not publicly available due to their considerable size but are available upon request from the corresponding author.

Supplementary Material

To view supplementary material for this article, please visit https://doi.org/10.1093/mam/ozaf013.

Acknowledgments

We thank Kathleen Bosmans (KU Leuven) for harvesting mouse auricles and Nicolas Charles-Pirlot (UCLouvain) for harvesting the human auricle. The X-ray microCT images were generated at the KU Leuven XCT Core Facility (supported by Jeroen Soete, research expert) and in the microCT lab of UCLouvain (Woluwe-Saint-Lambert, IREC). Bright-field images were acquired at the 2IP imaging platform of the UCLouvain (supported by Caroline Bouzin). This research was supported by the Research Foundation Flanders (FWO) through infrastructure grant I002720N. We thank Walid El Aazmani and Karem Tohala Pulgarin for their help with data acquisition. We thank Lieven Desmet, statistical consultant of the technological platform "Support en Méthodologie et Calcul Statistique," UCLouvain. Computational resources have been provided by the supercomputing facilities of the Université Catholique de Louvain (CISM/UCL) and the Consortium des Équipements de Calcul Intensif en Fédération Wallonie-Bruxelles (CÉCI) funded by the Fonds National de la Recherche Scientifique de Belgique (F.R.S.-FNRS) under convention 2.5020.11 and by the Walloon Region.

Author Contributions Statement

Conception and design: D.H. and G.K. Methodology: D.H., L.D., W.D.B., and G.K. Data acquisition and processing: D.H., T.B., S.V., L.P.M., A.M., and G.P. Writing: D.H., C.B., and G.K. Study supervision: G.K.

Financial Support

D.H. is a Postdoctoral Researcher of the Fonds National de la Recherche Scientifique—FNRS. T.B. is a FRIA grantee of the Fonds National de la Recherche Scientifique—FNRS. D.H., T.B., S.V., G.K., and W.D. acknowledge the support from an FWO project grant (G088218N). T.B., G.P., and G.K. acknowledge the support from the Action de Recherche Concertée (ARC 19/24-097), Fédération Wallonie-Bruxelles. A.M., G.P., and G.K. acknowledge the support from the SBO project of the Research Foundation Flanders (FWO, grant S007219N). L.D. is a senior research associate with the Fonds National de la Recherche Scientifique, Belgium. L.D. lab was funded by the FWO and F.R.S.-FNRS under the Excellence of Science Programme (EOS No. O.0006.22). The project was supported by the ASBL Jean Degroof-Marcel Van Massenhove funding and the Fondation Saint-Luc (RM2A project). Avizo 2022.1 (ThermoFisher Scientific, France) software acquisition was supported by the Fonds National de la Recherche Scientifique (FNRS-EQP-Tomo4D-U.N069.20).

Conflict of Interest

The authors declare that they have no competing interest.

References

Albers J, Svetlove A & Duke E (2024). Synchrotron X-ray imaging of soft biological tissues—Principles, applications and future prospects. *J Cell Sci* **137**(20), jcs261953. https://doi.org/10.1242/jcs.261953

Balcaen T, Piens C, Mwema A, Chourrout M, Vandebroek L, Des Rieux A, Chauveau F, De Borggraeve WM, Hoffmann D & Kerckhofs G (2023). Revealing the three-dimensional murine brain microstructure by contrast-enhanced computed tomography. *Front Neurosci* **17**, 1141615. https://doi.org/10.3389/fnins.2023.1141615

Ban S, Cho NH, Min E, Bae JK, Ahn Y, Shin S, Park S, Lee Y & Jung W (2019). Label-free optical projection tomography for quantitative three-dimensional anatomy of mouse embryo. *J Biophotonics* **12**, e201800481. https://doi.org/10.1002/jbio.201800481

Bock J, Guria S, Wedek V & Hennecke U (2021). Enantioselective dihalogenation of alkenes. *Chemistry* **27**, 4517–4530. https://doi.org/10.1002/chem.202003176

Brust H, Orzechowski S & Fettke J (2020). Starch and glycogen analyses: Methods and techniques. *Biomolecules* **10**, 1020. https://doi.org/10.3390/biom10071020

Busse M, Müller M, Kimm MA, Ferstl S, Allner S, Achterhold K, Herzen J & Pfeiffer F (2018). Three-dimensional virtual histology enabled through cytoplasm-specific X-ray stain for microscopic and nanoscopic computed tomography. *Proc Natl Acad Sci U S A* **115**, 2293–2298. https://doi.org/10.1073/pnas.1720862115

Buytaert J, Goyens J, De Greef D, Aerts P & Dirckx J (2014). Volume shrinkage of bone, brain and muscle tissue in sample preparation for micro-CT and light sheet fluorescence microscopy (LSFM). *Microsc Microanal* **20**, 1208–1217. https://doi.org/10.1017/S1431927614001329

Cesàro A, Crescenzi V, Delben F, Gamini A, Liut G, Paoletti S & Rizzo R (1992). Specific and non-specific ion-polysaccharide

Downloaded from https://academic.oup.com/mam/article/31/2/ozaf013/8104027 by guest on 23 May 2025

interactions. *Thermochim Acta* **199**, 1–15. https://doi.org/10.1016/0040-6031(92)80245-R

Cochez PM, Michiels C, Hendrickx E, Dauguet N, Warnier G, Renauld JC & Dumoutier L (2017). Ccr6 is dispensable for the development of skin lesions induced by imiquimod despite its effect on epidermal homing of IL-22-producing cells. *J Invest Dermatol* **137**, 1094–1103. https://doi.org/10.1016/j.jid.2016.12.023

Coleman R (2000). The impact of histochemistry—A historical perspective. *Acta Histochem* **102**, 5–14. https://doi.org/10.1078/0065-1281-00542

Dawood Y, Strijkers GJ, Limpens J, Oostra RJ & de Bakker BS (2020). Novel imaging techniques to study postmortem human fetal anatomy: A systematic review on microfocus-CT and ultra-high-field MRI. *Eur Radiol* **30**(4), 2280–2292. https://doi.org/10.1007/s00330-019-06543-8

De Bournonville S, Vangrunderbeeck S & Kerckhofs G (2019). Contrast-enhanced microCT for virtual 3D anatomical pathology of biological tissues: A literature review. *Contrast Media Mol Imaging* **2019**, 8617406. https://doi.org/10.1155/2019/8617406

de Bournonville S, Vangrunderbeeck S, Ly HGT, Geeroms C, De Borggraeve WM, Parac-Vogt TN & Kerckhofs G (2020). Exploring polyoxometalates as non-destructive staining agents for contrast-enhanced microfocus computed tomography of biological tissues. *Acta Biomater* **105**, 253–262. https://doi.org/10.1016/j.actbio.2020.01.038

De Clercq K, Persoons E, Napso T, Luyten C, Parac-Vogt TN, Sferruzzi-Perri AN, Kerckhofs G & Vriens J (2019). High-resolution contrast-enhanced microCT reveals the true three-dimensional morphology of the murine placenta. *Proc Natl Acad Sci U S A* **116**(28), 13927–13936. https://doi.org/10.1073/pnas.1902688116

Deyhle H, Schulz G, Khimchenko A, Bikis C, Hieber SE, Jaquiery C, Kunz C, Müller-Gerbl M, Höchel S & Saxer T (2016). Imaging tissues for biomedical research using the high-resolution micro-tomography system nanotom® m. In *Developments in X-Ray Tomography X*, vol. 9967, p. 99670Q. San Diego, California, United States: SPIE.

Dyer L, Parker A, Paphiti K & Sanderson J (2022). Lightsheet microscopy. *Curr Protoc* **2**, 448. https://doi.org/10.1002/cpz1.448

Early CM, Morhardt AC, Cleland TP, Milensky CM, Kavich GM & James HF (2020). Chemical effects of diceCT staining protocols on fluid-preserved avian specimens. *PLoS One* **15**, e0238783. https://doi.org/10.1371/journal.pone.0238783

Hanly A, Johnston RD, Lemass C, Jose A, Tornifoglio B & Lally C (2023). Phosphotungstic acid (PTA) preferentially binds to collagen-rich regions of porcine carotid arteries and human atherosclerotic plaques observed using contrast enhanced micro-computed tomography (CE-μCT). *Front Physiol* **14**, 1057394. https://doi.org/10.3389/fphys.2023.1057394

Jeffery NS, Stephenson RS, Gallagher JA, Jarvis JC & Cox PG (2011). Micro-computed tomography with iodine staining resolves the arrangement of muscle fibres. *J Biomech* **44**, 189–192. https://doi.org/10.1016/j.jbiomech.2010.08.027

Jing D, Yi Y, Luo W, Zhang S, Yuan Q, Wang J, Lachika E, Zhao Z & Zhao H (2019). Tissue clearing and its application to bone and dental tissues. *J Dent Res* **98**(6), 621–631. https://doi.org/10.1177/0022034519844510

Johnson JT, Hansen MS, Wu I, Healy LJ, Johnson CR, Jones GM, Capecchi MR & Keller C (2006). Virtual histology of transgenic mouse embryos for high-throughput phenotyping. *PLoS Genet* **2**, e61. https://doi.org/10.1371/journal.pgen.0020061

Joshi NS, Bansal PN, Stewart RC, Snyder BD & Grinstaff MW (2009). Effect of contrast agent charge on visualization of articular cartilage using computed tomography: Exploiting electrostatic interactions for improved sensitivity. *J Am Chem Soc* **131**, 13234–13235. https://doi.org/10.1021/ja9053306

Kalson NS, Malone PSC, Bradley RS, Withers PJ & Lees VC (2012). Fibre bundles in the human extensor carpi ulnaris tendon are arranged in a spiral. *J Hand Surg Eur Vol* **37**(6), 550–554. https://doi.org/10.1177/1753193411433228

Kang B, Tang H, Zhao Z & Song S (2020). Hofmeister series: Insights of ion specificity from amphiphilic assembly and interface property. *ACS Omega* **5**, 6229–6239. https://doi.org/10.1021/acsomega.0c00237

Kato CN, Shinohara A, Hayashi K & Nomiya K (2006). Syntheses and X-ray crystal structures of zirconium(IV) and hafnium(IV) complexes containing monovacant Wells–Dawson and Keggin polyoxotungstates. *Inorg Chem* **45**, 8108–8119. https://doi.org/10.1021/ic060656e

Kerckhofs G, Stegen S, van Gastel N, Sap A, Falgayrac G, Penel G, Durand M, Luyten FP, Geris L, Vandamme K, Parac-Vogt T & Carmeliet G (2018). Simultaneous three-dimensional visualization of mineralized and soft skeletal tissues by a novel microCT contrast agent with polyoxometalate structure. *Biomaterials* **159**, 1–12. https://doi.org/10.1016/j.biomaterials.2017.12.016

Koç MM, Aslan N, Kao AP & Barber AH (2019). Evaluation of X-ray tomography contrast agents: A review of production, protocols, and biological applications. *Microsc Res Tech* **82**, 812–848. https://doi.org/10.1002/jemt.23225

Leyssens L, Balcaen T, Pétré M, Béjar Ayllón N, El Aazmani W, de Pierpont A, Pyka G, Lacroix V & Kerckhofs G (2023). Non-destructive 3D characterization of the blood vessel wall microstructure in different species and blood vessel types using contrast-enhanced microCT and comparison with synthetic vascular grafts. *Acta Biomater* **164**, 303–316. https://doi.org/10.1016/j.actbio.2023.04.013

Leyssens L, Pestiaux C & Kerckhofs G (2021). A review of ex vivo X-ray microfocus computed tomography-based characterization of the cardiovascular system. *Int J Mol Sci* **22**(6), 3263. https://doi.org/10.3390/ijms22063263

Litzlbauer HD, Neuhaeuser C, Moell A, Greschus S, Breithecker A, Franke FE, Kummer W & Rau WS (2006). Three-dimensional imaging and morphometric analysis of alveolar tissue from microfocal X-ray-computed tomography. *Am J Physiol Lung Cell Mol Physiol* **291**, L535–L545. https://doi.org/10.1152/ajplung.00088.2005

Lombardi S, Scola E, Ippolito D, Zambelli V, Botta G, Cuttin S, Triulzi F & Lombardi CM (2019). Micro-computed tomography: A new diagnostic tool in postmortem assessment of brain anatomy in small fetuses. *Neuroradiology* **61**, 737–746. https://doi.org/10.1007/s00234-019-02168-2

Maes A, Pestiaux C, Marino A, Balcaen T, Leyssens L, Vangrunderbeeck S, Pyka G, De Borggraeve WM, Bertrand L, Beauloye C, Horman S, Wevers M & Kerckhofs G (2022). Cryogenic contrast-enhanced microCT enables nondestructive 3D quantitative histopathology of soft biological tissues. *Nat Commun* **13**(1), 6207. https://doi.org/10.1038/s41467-022-34048-4

McLaughlin AI, Milton R & Perry KM (1946). Toxic manifestations of osmium tetroxide. *Occup Environ Med* **3**, 183–186. https://doi.org/10.1136/oem.3.3.183

Messal HA, Almagro J, Zaw Thin M, Tedeschi A, Ciccarelli A, Blackie L, Anderson KI, Miguel-Aliaga I, van Rheenen J & Behrens A (2021). Antigen retrieval and clearing for whole-organ immunofluorescence by FLASH. *Nat Protoc* **16**, 239–262. https://doi.org/10.1038/s41596-020-00414-z

Metscher BD (2009). MicroCT for developmental biology: A versatile tool for high-contrast 3D imaging at histological resolutions. *Dev Dyn* **238**, 632–640. https://doi.org/10.1002/dvdy.21857

Michiels C, Puigdevall L, Cochez P, Achouri Y, Cheou P, Hendrickx E, Dauguet N, Blanchetot C & Dumoutier L (2021). A targetable, non-canonical signal transducer and activator of transcription 3 activation induced by the Y-less region of IL-22 receptor orchestrates imiquimod-induced psoriasis-like dermatitis in mice. *J Invest Dermatol* **141**, 2668–2678.e6. https://doi.org/10.1016/j.jid.2021.04.016

Musumeci G (2014). Past, present and future: Overview on histology and histopathology. *J Histol Histopathol* **1**, 5. https://doi.org/10.7243/2055-091X-1-5

Downloaded from https://academic.oup.com/mam/article/31/2/ozaf013/8104027 by guest on 23 May 2025

Ribi W, Senden TJ, Sakellariou A, Limaye A & Zhang S (2008). Imaging honey bee brain anatomy with micro-X-ray-computed tomography. *J Neurosci Methods* **171**, 93–97. https://doi.org/10.1016/j.jneumeth.2008.02.010

Sanzone CF & Reith EJ (1976). The development of the elastic cartilage of the mouse pinna. *Am J Anat* **146**, 31–71. https://doi.org/10.1002/aja.1001460103

Starovoyt A, Shaheen E, Putzeys T, Kerckhofs G, Politis C, Wouters J & Verhaert N (2023). Anatomically and mechanically accurate scala tympani model for electrode insertion studies. *Hear Res* **430**, 108707. https://doi.org/10.1016/j.heares.2023.108707

Stewart RC, Patwa AN, Lusic H, Freedman JD, Wathier M, Snyder BD, Guermazi A & Grinstaff MW (2017). Synthesis and preclinical characterization of a cationic iodinated imaging contrast agent (CA4+) and its use for quantitative computed tomography of ex vivo human hip cartilage. *J Med Chem* **60**(13), 5543–5555. https://doi.org/10.1021/acs.jmedchem.7b00234

Stockwell RA (1965). Lipid in the matrix of ageing articular cartilage. *Nature* **207**(995), 427–428. https://doi.org/10.1038/207427a0

Thoma JA & French D (1960). The starch-iodine-iodide interaction. Part I. Spectrophotometric investigations. *J Am Chem Soc* **82**, 4144–4147. https://doi.org/10.1021/ja01501a004

Thompson N, Ravagli E, Mastitskaya S, Iacoviello F, Aristovich K, Perkins J, Shearing PR & Holder D (2020). MicroCT optimisation for imaging fascicular anatomy in peripheral nerves. *J Neurosci Methods* **338**, 108652. https://doi.org/10.1016/j.jneumeth.2020.108652

Titford M (2006). A short history of histopathology technique. *J Histotechnol* **29**(2), 99–110. https://doi.org/10.1179/his.2006.29.2.99

Titford M (2009). Progress in the development of microscopical techniques for diagnostic pathology. *J Histotechnol* **32**, 9–19. https://doi.org/10.1179/his.2009.32.1.9

Van Belle AB, de Heusch M, Lemaire MM, Hendrickx E, Warnier G, Dunussi-Joannopoulos K, Fouser LA, Renauld J-C & Dumoutier L (2012). IL-22 is required for imiquimod-induced psoriasiform skin inflammation in mice. *J Immunol* **188**, 462–469. https://doi.org/10.4049/jimmunol.1102224

Vickerton P, Jarvis J & Jeffery N (2013). Concentration-dependent specimen shrinkage in iodine-enhanced microCT. *J Anat* **223**, 185–193. https://doi.org/10.1111/joa.12068

Waarsing J, Mc E, Day JS & Weinans H (2005). Longitudinal micro-CT scans to evaluate bone architecture porous biomaterials view project 3D acetabular cup orientation in total hip arthroplasty view project. *J Musculoskelet Neuronal Interact* **5**(4), 310. https://www.ismni.org/jmni/article/5/310

Walsh CL, Tafforeau P, Wagner WL, Jafree DJ, Bellier A, Werlein C, Kühnel MP, Boller E, Walker-Samuel S, Robertus JL, Long DA, Jacob J, Marussi S, Brown E, Holroyd N, Jonigk DD, Ackermann M & Lee PD (2021). Imaging intact human organs with local resolution of cellular structures using hierarchical phase-contrast tomography. *Nat Methods* **18**(12), 1532–1541. https://doi.org/10.1038/s41592-021-01317-x

Yamazaki T, Li W, Yang L, Li P, Cao H, Motegi SI, Udey MC, Bernhard E, Nakamura T & Mukouyama YS (2018). Whole-mount adult ear skin imaging reveals defective neuro-vascular branching morphogenesis in obese and type 2 diabetic mouse models. *Sci Rep* **8**(1), 430. https://doi.org/10.1038/s41598-017-18581-7

Yu T, Zhu J, Li D & Zhu D (2021). Physical and chemical mechanisms of tissue optical clearing. *iScience* **24**, 102178. https://doi.org/10.1016/j.isci.2021.102178

Downloaded from https://academic.oup.com/mam/article/31/2/ozaf013/8104027 by guest on 23 May 2025